JOURNAL OF PROPULSION AND POWER
Vol. 24, No. 5, September–October 2008

Experimental Investigation of a Two-Dimensional and a Three-Dimensional Scramjet Inlet at Mach 7

J. Häberle* and A. Gülhan†
DLR, German Aerospace Center, 51147 Cologne, Germany

DOI: 10.2514/1.33546

The current experimental study at Mach 7 was carried out to investigate the viscous flow effects in a scramjet inlet with a fixed geometry operating at Mach 7.5–8. To reduce the risk of inlet unstart, an optional passive boundary-layer bleed was integrated at the throat and tested for different bleed dimensions. The passive bleed significantly reduces the lip-shock-induced separation bubble on the ramp. But the correct location of the bleed gap is important for the reduction of the separation bubble. To investigate the compression behavior, different backpressures were applied and the effects on the internal flow structure were analyzed by means of static pressure along the isolator and pitot pressure profiles at the exit of the isolator. Because the reference configuration has a very small internal contraction ratio to guarantee self-starting, the internal compression ratio was increased in three steps by means of additional sidewall compression along the internal flowpath. This includes internal contraction ratios above the starting limit. This measure led to a significant increase of the static pressure ratio at the end of the isolator. The complex flow structures are explained by means of detailed static and pitot pressure plots.

Nomenclature

A	=	area, m^2
c_p	=	pressure coefficient, $(p - p_\infty) \cdot q_\infty^{-1}$
I	=	internal compression, $1 - (A_{th} \cdot A_{lib}^{-1})$
L	=	length, m
M	=	Mach number
$\dot{m}$	=	mass flow, kgs^{-1}
p	=	pressure, Nm^{-2}
q	=	dynamic pressure, Nm^{-2}
R	=	specific gas constant for air 287.15, $Jkg^{-1}K^{-1}$
Re	=	Reynolds number
T	=	temperature, K
α	=	calibration value
Δ	=	throttle degree, $(1 - (A_{mfm,th} \cdot A_0^{-1})) \cdot 100\%$
ρ	=	density, kgm^{-3}
π	=	total pressure recovery

Subscripts

CC	=	combustion chamber entry condition
mfm	=	mass flow meter
SW	=	sidewall compression inlays 1 and 2
th	=	throat
$t0$	=	wind-tunnel total conditions
w	=	wall
0	=	freestream plane ahead of the inlet
∞	=	wind-tunnel freestream conditions

I. Introduction

TO CONSOLIDATE the database of scramjet inlets, further studies have been performed on a previously investigated 2-D inlet [1] to consider the effects of passive bleed configurations and different internal contraction ratios in more detail. Compared with previously investigated hypersonic inlet models for a Mach number of $M = 6$ [2], the present $M = 7.5$–8 model is equipped with more static pressure ports and better optical access. In addition, with the results obtained from the 2-D inlet published in [1], this extended database help to improve the design of scramjet propulsion inlets for future hypersonic single-stage-to-orbit and two-stage-to-orbit space vehicles for the access to space or hypersonic transportation.

The paper first focuses on a 2-D double-wedge ramp configuration with a horizontal lip designed by oblique shock theory and the method of characteristics using an existing tool proposed by Anderson [3]. The horizontal lip results in a relatively strong lip shock impinging on the ramp boundary layer, ultimately forcing the boundary layer to separate. As a consequence, a large separation bubble emerges in the throat of the inlet. To influence the viscous interaction, a passive boundary-layer bleed is integrated in the model design. The bleed-gap size and position are variable, and the effects of this bleed on the flow structure and the necessity of such a device will be discussed in the present paper. Differences to previous bleed investigations for flat plates (i.e., Schulte et al. [4]) are shown and discussed. The importance is shown of placing the bleed at the right location and dimensioning the bleed gap accordingly. Computations for a single bleed hole in a flat plate and an impinging shock were performed by Shih et al. [5]. The paper reveals the physical mechanisms and the influence lengths of bleed holes near incident shocks. Harloff and Smith [6] developed an analytical method to design boundary-layer bleed holes and slots. Downstream of the inlet throat, the isolator connects the inlet with the combustion chamber and adapts the flow in terms of static pressure delivered by the inlet to the static pressure in the combustion chamber. This is accomplished by a so called shock train, a system of oblique or normal shocks that has been investigated in detail for symmetric inflow conditions (e.g., by Billig and Kothari [7] and Billig [8]) and is also described in the standard textbook by Heiser and Pratt [9]. Depending on the combustion-chamber static pressure, the flow structure in the isolator varies (Sugiyama et al. [10]). For a scramjet compression setup with nonsymmetric inflow conditions to the isolator, the flow structure is visualized (i.e., by Hermann and Koschel [11] and Reinartz et al. [12]) for different backpressures. These different structures are investigated and discussed in this paper by means of pitot pressure measurements and static pressure measurements, with the focus on the bleed effects.

Second, the internal contraction ratio is increased by reducing the width of the model by introducing sidewall compression inlays in the

Received 1 August 2007; revision received 28 April 2008; accepted for publication 5 May 2008.

*Ph.D. Student, Wind Tunnel Department, Institute of Aerodynamics and Flow Technology, Linder Höhe. Student Member AIAA.

†Head of Department, Wind Tunnel Department, Institute of Aerodynamics and Flow Technology, Linder Höhe. Member AIAA.

region of the isolator. Thus, the internal compression region of the inlet is increased and the isolator length is reduced. Two different sets of inserts were used to adjust the internal contraction ratio slightly below and above the Kantrowitz limit as detailed in [13], as described next. This was done to evaluate the limits of this well-known criterion for combined compression systems with thick boundary layers and 3-D corner flows. The performance of a hypersonic inlet is not necessarily described by the total pressure recovery, but more by the static pressure rise the inlet can deliver to the combustion chamber without any shock train and the static temperature. Thus, it is very important for the design of hypersonic intakes to know how many of the wanted compression can be accomplished with internal compression, because pure external compression would lead to steeper ramp angles and the reverse deflection of the flow would be more complex (i.e., internal flowpath with constant area, increased cowl drag, etc.). Because the emerging flow phenomena are very complex (especially the viscous effects, which are not taken into account by most early-phase design tools, such as [13] in the present case), it is absolutely necessary to have a reliable experimental database. This database can then be used to achieve more confidence in estimating allowable internal contraction ratios during the optimization phase with inviscid computations and, more important, to validate CFD tools and the used turbulence models for more detailed evaluation of the performance of the inlet design.

Pure sidewall compression systems have been investigated in great detail by Holland and Murphy [14] and Holland [15] by means of pressure plots and oil-flow photographs and by Tani et al. [16], showing the crossing shock system. Zuber et al. [17] investigated the flowfield structure for crossing shocks for different sidewall contraction ratios and described the heat flux distribution on the base plate and the complex vortex structure. Introducing sidewall compression leads to a very complex 3-D shock interaction pattern. In the past, various 3-D wedge compression configurations have been investigated (e.g., the groups in Novosibirsk, Russia [18] and in China [19]). Currently, full 3-D compression systems are investigated in the HYCAUSE project, as reported by Walker [20] and thermally analyzed by Ho [21]. Smart et al. [22–24] published a series of papers discussing the design for rectangular to elliptical shape inlets.

The goals of the recent experimental program and the main focus in this paper were as follows:

1) Measure the effects of different integrated passive boundary-layer bleed configurations at the location of the lip-shock impingement on pressure distribution, Mach number distribution, and combustion-chamber mass flow.

2) Increase the internal contraction ratio by means of reducing the inlet isolator width.

II. Experimental Tools

A. Wind-Tunnel and Test Conditions

The current experiments were conducted in the hypersonic wind tunnel H2K in Cologne, Germany. The facility is equipped with five contoured nozzles with an exit diameter of 600 mm (i.e., $M = 5.3, 6, 7, 8.7$, and 11.2). For the experiments of this study, the Mach 7 nozzle was used. The working principle is a blowdown wind tunnel with test durations, depending on the flow conditions, of up to 30 s. To avoid condensation and to operate the wind tunnel at different stagnation temperatures, the air is heated by electrical heaters with a heating capacity of up to 5 MW. During the heating process the air is blown to the atmosphere until the desired stationary stagnation temperature is reached; subsequently, a $3/2$ valve is activated to let the air flow through the nozzle into the vacuum dump tank. The range of achievable Mach numbers and Reynolds numbers, as well as a picture of the test section, can be seen in Fig. 1. Reynolds numbers between 2.5×10^6 and 20×10^6 m^{-1} can be set by varying the stagnation pressure and stagnation temperatures.

The wind-tunnel flow conditions for the current test campaign are summarized in Table 1 and are also displayed in the performance map of the wind tunnel in Fig. 1.

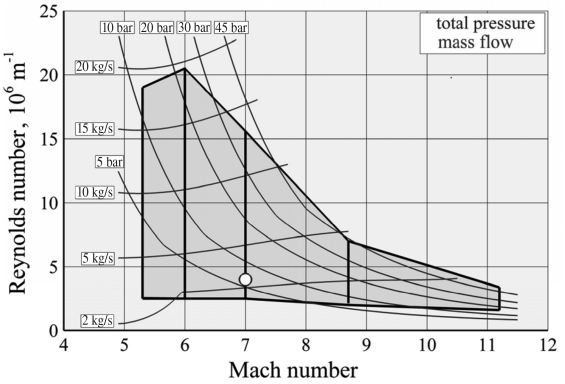

Fig. 1 Hypersonic wind tunnel H2K performance map.

B. Inlet Model

The basic 2-D configuration is self-starting according to the Kantrowitz limit as detailed in [13] and was developed based on the previously developed $M = 6$ SCR-02 model [2]. To achieve a sufficient combustion-chamber height and the demanded reduced internal compression and to maintain the horizontal lip, the throat height had to be increased, resulting in a reduced second ramp length, as seen in Fig. 2. The second ramp and the horizontal throat are connected by means of an arc.

Because of the horizontal lip, which results in a strong lip shock impinging on the ramp boundary layer, this configuration leads to a separation bubble in the throat region of the inlet. Therefore, the model was designed with an optional passive boundary-layer bleed (dashed line in Fig. 2) to prevent a possible unstart of the inlet. The bleed-slot dimensions were variable in the x position as well as in bleed-gap size. The bleed gap could be placed at $x = 410$, 415, and 420 mm, with bleed-gap sizes ranging from 10, 15, to 20 mm. All possible bleed configurations are summarized in Table 2. Configurations 0 and 1 are described in detail in [1].

The capture area A_0 of the model is 0.1×0.1 m^2 and the length to the defined interface to the combustion chamber is $L = 0.585$ m. It is equipped with a pitot rake consisting of five pitot tubes at the inlet/combustion-chamber interface, 17 static pressure ports in the upper wall of the isolator (H1-H17), and 25 pressure ports at the lower isolator wall, including six pressure ports on the external ramps (R1-R25) and a total of four optical windows, which are integrated in a way that the complete internal flowpath can be observed (see Fig. 2). Compared with the previous model, this model offers better measurement possibilities and more flexibility in configuration changes [2].

The basic configuration with an isolator width of $W = 100$ mm (2-D inlet) has an internal contraction ratio of $I = 16\%$. This is well below the Kantrowitz limit as detailed in [13], which is $I = 34\%$ for the corresponding lip Mach number. Thus, a starting device (i.e., a movable ramp or lip) is not necessary. Instead of the optical windows, metallic inserts could be installed to vary the width of the internal part of the inlet from $W = 100$ to 80 and 70 mm, respectively. The width of the inlet is unchanged up to $x = 0.410$ m and the reduced width is reached at $x = 0.500$ m, resulting in a sidewall ramp angle of $\delta_{SW1} = 6.4$ deg and $\delta_{SW2} = 9.5$ deg. This leads to an increase in internal contraction ratio from $I = 16$ to 31 and

Table 1 Wind-tunnel flow conditions

Wind-tunnel parameter	Value
Freestream Mach number M_∞	7
Freestream pressure p_∞, Pa	163
Freestream temperature T_∞, K	46
Freestream density ρ_∞, kgm^{-3}	0.0118
Total temperature T_{t0}, K	500
Total pressure p_{t0}, Pa	7.0×10^5
Unit Reynolds number Re_m, m^{-1}	4×10^6

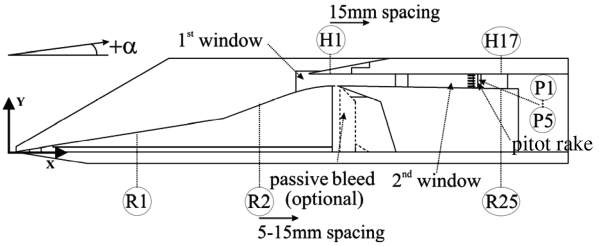

Fig. 2 Side view of the inlet model with integrated passive bleed.

39% (see Fig. 3). The pitot rake can be placed on the centerline and ±25 mm offaxis positions at $z = 25, 50\ (C/L)$, and 75 mm.

The inlet model itself is attached to the settling chamber of the flow meter. At the interface, the transition from rectangular to round channel shape is accomplished.

III. Measurement Techniques and Data Reduction

The hypersonic wind-tunnel facility uses a coincident shadowgraph optical setup to visualize the flow around and in the inlet model. In combination with a very light-sensitive charge-coupled-device camera, the optical path could be modified from a prism to a beam-splitter shadowgraph setup [25]. The static pressures and the pitot pressure measurements are made with the commercial Pressure Systems, Inc. (PSI), 8400 system using a 64-PSI module in the present measurement campaign.

A rotational symmetric flow meter with a conical plug was used to measure the captured flow rate [2,26] and to simulate the pressure induced by the combustion chamber. The theory, which is used to evaluate the mass flow rate, assumes a one-dimensional flow without heat addition and sonic condition at the throat.

Calibration of the whole measurement setup is needed in advance, in accordance with DIN-1952 [27], to achieve a relation between measured mass flow and actual mass flow as a function of throat area. The calibration factor α varies between $0.99 < \alpha < 1.02$ in the region of interest. The captured mass is corrected by means of this calibration function to determine the correct captured mass flow. The mass capture ratio (MCR) of the inlet is defined as

$$\mathrm{MCR} = \frac{\dot{m}_{\mathrm{mfm}}}{\dot{m}_0} = \frac{\dot{m}_{\mathrm{CC}}}{\dot{m}_0} \tag{1}$$

The calculation of the captured mass flow can be divided into three steps.

1) The throat area of the flow meter is calculated based on the measured lateral position of the conical plug and the known geometrical dimensions of the mass flow meter.

2) The Mach number M_{mfm3} ahead of the conical plug is iteratively calculated by solving the appropriate equation.

Table 2 Investigated model bleed configurations

Bleed configuration	Bleed width	Bleed start location	Bleed-gap size
0	100 mm	no	no
1	100 mm	$x = 0.410$ m	$t = 10$ mm
2	100 mm	$x = 0.410$ m	$t = 15$ mm
3	100 mm	$x = 0.410$ m	$t = 20$ mm
4	100 mm	$x = 0.420$ m	$t = 10$ mm

3) The captured mass flow is calculated using the measured static pressure p_{mfm3} in front of the conical plug, the calculated Mach number, and the known total temperature, according to Eq. (2).

The static pressure p_{mfm3} is measured at four locations on the circumference of the settling chamber and then averaged. In addition, two thermocouples are integrated in the settling chamber to measure the total temperature in front of the conical plug. A constant factor $F = 0.934$ was obtained to take into account the total temperature decrease by analyzing wind-tunnel total temperature and mass flow meter total temperature, which is accurate within ±1.6% for all test runs in the present measurement campaign.

$$\dot{m}_{\mathrm{mfm}} = \frac{1}{F}\frac{1}{\alpha}\frac{p_{\mathrm{mfm3}}}{\sqrt{RT_{t0}}}A_{\mathrm{mfm3}}\sqrt{(1 + \frac{k-1}{2}M^2_{\mathrm{mfm3}})} \tag{2}$$

The theoretically captured mass flow is calculated by the well-known total conditions in the freestream and the capture area of the inlet. Finally, the mass capture ratio is calculated from Eq. (1).

In addition to evaluating the captured mass flow of the inlet, the mass flow meter is also used to apply different backpressures to the inlet flow. The backpressure is measured at the pitot rake position and is calculated as the mean value of the upper and lower static pressure values at this location. All experimental uncertainties are summarized in Table 3; the calibrated nozzle exit Mach number based on the investigated unit Reynolds number is used for the uncertainty calculations and is assumed to be known.

IV. Experimental Results

A. Two-Dimensional Inlet, Width of 100 Millimeters

1. *Backpressure Ratio Variation with Different Throttle Degrees*

Different backpressures are imposed on the internal flowfield of the scramjet compression system by means of the attached mass flow meter. The relation between the throttle degree Δ and the backpressure ratio can be seen in [1] for configurations 0 and 1. Without any backpressure imposed by the mass flow meter $\Delta < 75\%$, the static pressure ratio at the position of the pitot rake is $p/p_\infty = 30$. The pressure ratio generally increases with increasing throttling degree. For $\Delta > 84\%$, the flow at the defined combustion-chamber interface $x = 0.585$ m is completely subsonic. At $\Delta \approx 85$–86%, which corresponds to $p/p_\infty \approx 160$–180, the flow in the inlet throat is still supersonic and the inlet is started, but the

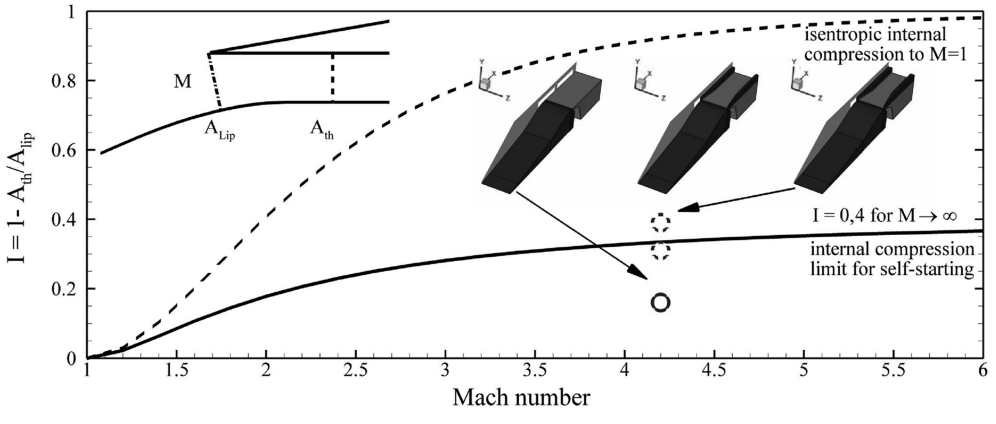

Fig. 3 Internal compression ratio for the three investigated inlet configurations, comparison with the Kantrowitz limit as detailed in [13].

Table 3 Experimental uncertainties

Wind-tunnel parameter	Value	Uncertainties
Freestream Mach number M_∞	7	±0.714%
Total temperature T_{t0}, K	500	±0.75%
Total pressure p_{t0}, Pa	7.0×10^5	±0.0397% (20 bar)
Mass capture ratio	MCR	±2.8%
Pitot-pressure coefficient	$c_{p,\text{pitot}}$	±3.4%
Calculated pitot Mach number	M	±5%
Static pressure coefficient	c_P	±3.8–5.6%
Backpressure ratio	p/p_∞	±2.11%
Geometrical resolution	x, y, z	0.05 mm

flow inside the complete isolator is subsonic. The inlet blockage starts at $\Delta > 86\%$. The backpressure behavior is described in more detail in [1].

2. Pressure Distribution and Shadowgraph Picture for Different Bleed Configurations

The basic configuration without bleed and with a 10-mm bleed gap at $x = 0.410$ m has been investigated in detail and is described in [1]. The pressure distribution for cases 2 and 3 compared with case 1 is very similar, especially up to $x = 0.500$ m. The shock-induced boundary-layer separation has vanished and the pressure on the upper wall decreases with an increasing x coordinate. The same is true for the two investigated cases with a bleed gap of 15 and 20 mm, as can be seen in Fig. 4. The flow structures in the shadowgraphs look very similar. The lip shock falls in the bleed gap, and the bleed-gap-induced shock leads to a separation bubble on the upper wall in the region $0.450 \text{ m} < x < 0.490$ m. The position moves slightly downstream as the bleed gap moves downstream. As a result of the separation bubble on the upper wall, a two-shock system propagates downstream in the isolator: the separation shock and the reattachment shock. Both shocks and the reflected shocks are visible in Fig. 4 for both bleed configurations. The difference between no bleed and any of the investigated bleed configurations 2 and 3 (see Fig. 4) are obvious (see [1] for configurations 0 and 1).

For both bleed configurations, different backpressure ratios were applied to simulate the increase in combustion-chamber pressure. The pressure ratio for no additional imposed backpressure for the 15-mm bleed gap is approximately the same as for the configurations described in [1]. This is based on the small differences in mass flow (see Table 4). The upstream propagation of the shock train in the isolator for increasing backpressure ratio is clearly seen in Fig. 4a. In general, the pressure rises more smoothly on the lower wall (dashed

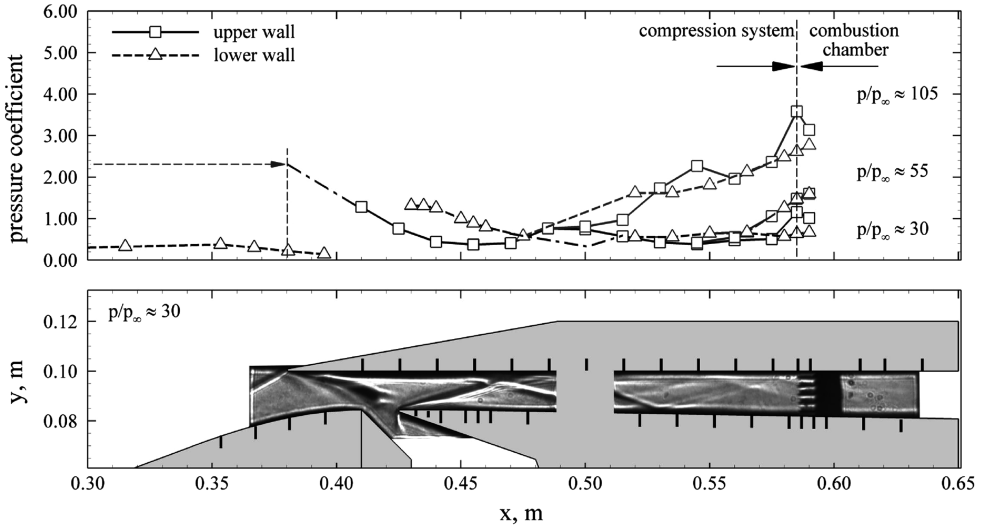

a) Bleed gap at x=410 mm and t=15 mm

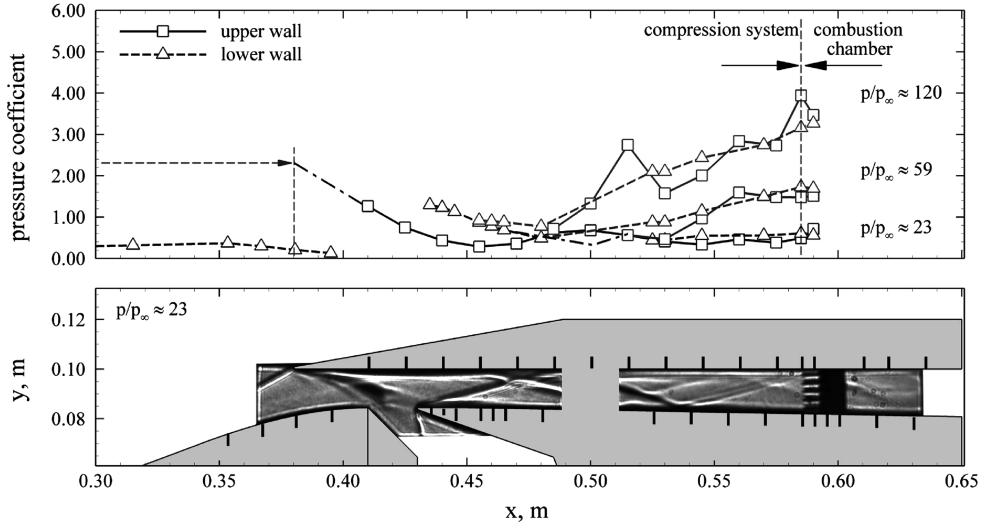

b) Bleed gap at x=410 mm and t=20 mm

Fig. 4 Comparison of the static wall pressures in the isolator with different bleed configurations including the theoretical pressure value at the lip tip computed by oblique shock theory, shadowgraph picture with no additional imposed backpressure $p/p_\infty = 30$.

Table 4 Breakdown of the different inlet mass flows and total pressure recovery

	Mass flow rate			π
Bleed configuration	MCR	Bleed mass flow ratio	Spill mass flow ratio	p_{t3}/p_{t0}
0	$0,71 \pm 2,8\%$	0	0.29	0.12
1	$0,69 \pm 2,8$	0.02	0.29	0.11
2	$0,68 \pm 2,8\%$	0.03	0.29	0.135
3	$0,64 \pm 2,8\%$	0.07	0.29	0.134
4	$0,68 \pm 2,8\%$	0.03	0.29	0.14

lines) than on the upper wall (solid line) (Figs. 4a and 4b). This is based on the fact that the flow is not symmetric in the isolator, due to the reflected lip shock and the opening angle at the lower wall of 1 deg. The thickening of the boundary layer is more distinct at the lower wall, thus resulting in a supersonic jet with shock-train structures in the upper part of the isolator. The shocks of the shock train lead to a stronger variation in wall pressure on the upper wall. This is in contrast to experiments with a direct connected-pipe test setup and symmetric inflow conditions.

The diverted mass flow for the 20-mm bleed gap is considerably higher than in the previous cases (see Table 4). This is the reason for the reduced pressure ratio of only $p/p_\infty = 23$ and the difference in the pitot rake results, which are discussed later. The most obvious effect of this reduced pressure rise is visible when different backpressures are applied (see Fig. 4b). The second backpressure value of $p/p_\infty = 59$ is very close to that in Fig. 4a ($p/p_\infty = 55$), but the pressure rise occurs much further upstream than in the case for the 15-mm bleed gap. This is based on the fact that the shock train needs more space (the backpressure propagates further upstream in the subsonic boundary layer) to raise the pressure in the isolator to the preset combustion-chamber pressure. Comparing the pressure plots leads to an approximate starting point of the shock train for the 15-mm bleed gap of $x = 0.560$ m (see Fig. 4a), and the starting point of the shock train for the 20-mm bleed gap is $x = 0.510$ m (see Fig. 4b). This means that the shock-train length has approximately tripled.

The variation of flow structure due to the different bleed configurations is also discussed by means of the pitot rake results (see Fig. 5). The pitot pressure profiles for no bleed and a 10-mm bleed gap are compared and discussed in [1]. The differences are only minor in terms of profile. The maximum pitot pressure without additional imposed backpressure is approximately $c_{p,\text{pitot}} = 11.5$ for no bleed and $c_{p,\text{pitot}} = 9$ for 10-mm bleed-gap configurations. The maximum Mach number for these configurations is approximately $M = 2.7$.

Looking at the pitot pressure results for the two bleed configurations 2 and 3 in more detail reveals some differences. The maximum pitot pressure for the 15-mm bleed-gap configuration is approximately the same, but further decreases for the 20-mm bleed gap. In addition, the pressure profiles also change in a way that the pressure profiles become more and more symmetric to the isolator horizontal symmetry line for no imposed backpressure (square symbols) (compare configurations 0 and 1 [1] and 2 and 3 in Fig. 5). Nevertheless, for increasing backpressure ratios, the profiles become asymmetrical again. This is another indication that the asymmetry is induced by the very small opening angle of the lower isolator wall of 1 deg. This is not the case for direct connected-duct isolator tests with homogeneous flow and different backpressures (as reported, for example, by Lin et al. [28]). Here, the pitot pressure, Mach number, and temperature profiles remain symmetric. So it seems that the flow structure is very sensitive to defined geometry variations of the isolator and the isolator inflow conditions, which means that the flow might also be very sensitive to small changes based on, for example, thermal and mechanical deformation during flight, manufacturing tolerances, etc. The subsonic region is bigger in the lower half of the isolator and the supersonic jet is located more in the upper half of the isolator, as can be seen in the pitot pressure distribution and the calculated Mach number profiles in Fig. 5. This matches the previously discussed differences in smoothness of the static pressure distribution.

The Mach number is calculated using the upper-wall static pressure value for the two upper pitot tubes, the lower wall static pressure value for the two lower pitot tubes, and the mean value for the middle pitot tube. The error bars indicate possible variations in the static pressure value and are on the order of $\pm 5\%$. Comparing the calculated Mach number profiles, it is obvious that the Mach number profile has approximately the same shape as the 10-mm bleed-gap configuration discussed in [1]. The maximum Mach number is approximately $M = 2.8$, compared with $M = 2.7$. The Mach number decreases with increasing backpressure ratio, and for the $p/p_\infty = 105$ case, most of the isolator flow is subsonic.

The calculated Mach number profile for the 20-mm gap configuration looks slightly different for the case with no additional imposed backpressure. The maximum Mach number is considerably higher: $M = 3.4$. This is based on the fact that the compression ratio is decreased, due to the lower mass flow through the isolator, resulting in a higher Mach number. Increasing the backpressure also results in a decrease in Mach number. For the backpressure ratio of $p/p_\infty = 59$, the Mach number decreases even more (compare Figs. 5a and 5b). This is based on the aforementioned longer shock train that is required to reach approximately the same backpressure ratio; thus, the aforementioned statement is confirmed. The next pressure ratios ($p/p_\infty = 105$ and 120) lead to almost complete subsonic flow in the isolator exit plane for both configurations. The higher obtainable pressure ratio for bleed configuration 2 is based on the same rational as before.

Next, the effects of maintaining a 10-mm bleed-gap size as discussed in [1], but moving the bleed downstream from $x = 0.410$ to 0.420 m, will be discussed. In the literature, various optimized bleed-gap locations in relation to the inviscous impinging shock are discussed [29,30], but mainly for shocks impinging on flat plates. One result by Schulte et al. [29] for a shock impinging on a flat plate is that the bleed should be located slightly upstream of the inviscous impinging shock location. In the present case, the lip shock impinges (based on method-of-characteristics calculations) at $x = 0.430$ m; thus, the selected positioning for the bleed at $x = 0.420$ m and 10-mm gap size meets the recommendations. The effect of placing the bleed in this location is visible in Fig. 6. Based on the thick-ramp boundary layer, the lip shock impinges on the ramp in front of the bleed. Thus, the pressure rise in the x direction forces the boundary layer to separate in front of the bleed and to propagate further upstream. The existence of a separation bubble is not only visible in the shadowgraph pictures, but also by looking at the static pressure plot. The value of the last pressure port on the ramp is increased, and the pressure rise due to the boundary-layer-induced shock impinging on the upper wall is also notable (compare Fig. 6 to the situation shown in Fig. 4).

These observations show that this bleed location is not positioned well and that the chosen bleed location for the basic configuration 1 discussed in [1] is more effective. Of course, the conclusions by Schulte et al. [29] were correct for the flat plate they investigated. This example shows that it is difficult to transfer results from different experimental configurations.

In Table 4, the breakdown of the different mass flows is shown. The captured mass flow for the started inlet without boundary-layer bleed is $\dot{m}_{CC}/\dot{m}_0 = 0.71$ and the spill is consequently $\dot{m}_{\text{spill}}/\dot{m}_0 = 0.29$. The reason for this large spill is described in [1]. The feasibility of the mass flow meter measurement was checked by means of computational fluid dynamics (CFD) calculations. The method-of-characteristics design with a sharp leading edge predicted

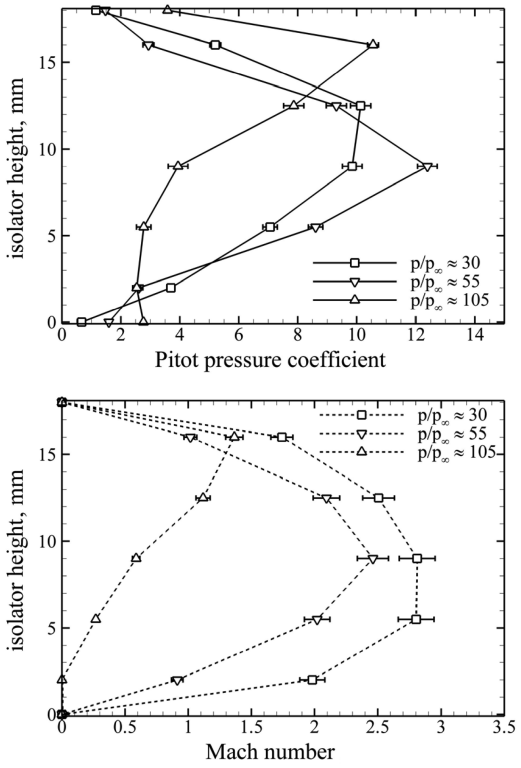

a) Bleed configuration 2, x = 0.410 m and 15-mm gap

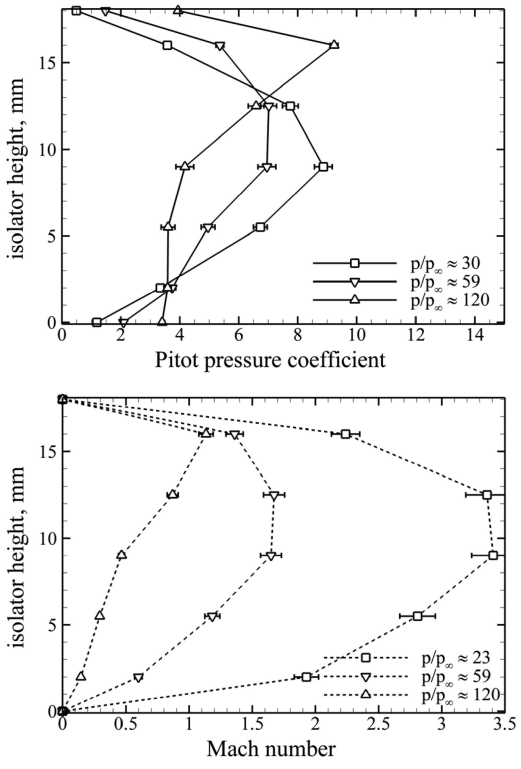

b) Bleed configuration 3, x = 0.410 m and 20-mm gap

Fig. 5 Comparison of the pitot pressure profiles and the calculated Mach number profiles over the height of the isolator exit at $x = 0.585$ m.

$\dot{m}_{CC}/\dot{m}_0 = 0.82$, which is obviously too high. A 3-D Speciale–Sakar–Gatski calculation accomplished by university partners with the FLOWer code [31] results in a mass capture ratio of $\dot{m}_{CC}/\dot{m}_0 = 0.69$, which is an acceptable agreement. Because the inlet did not block for either configuration, the spill is assumed to be identical for both configurations. This leads to the result that the removed mass flow by the passive bleed is on the order of $\dot{m}_{bleed}/\dot{m}_0 = 0.02$ for configuration 1, as shown in Table 2. The bleed mass flow is very small for all configurations.

As already mentioned, for this investigation, the external spill is held constant and one can see that the bleed spilled mass flow increases 50% linearly to an increase of 50% in gap size (configuration 1 to configuration 2). In contrast, the bleed mass flow increases approximately 250%, compared with an increase of 100% in gap size (configuration 1 to configuration 3). This is based on the fact that the shape of the lip shock is more or less unaffected by the bleed-gap size and turns the ramp flow into the direction of the bleed gap. This turning requires a certain radius and is always the same for the three cases (1, 2, and 3). Because the first bleed configuration is placed in a way that the lip shocks impinges in the middle of the gap, only boundary-layer flow with limited mass flow is swallowed by the bleed. For an increase of 5 mm (configuration 2), the same is basically true. Nevertheless, a greater boundary-layer mass flow is removed, because the dividing streamline to the downstream corner of the bleed is located further away from the ramp wall. The bleed size for configuration 3 is so big that mainstream mass is swallowed, in addition to the boundary-layer mass flow, thus increasing the bleed total mass flow for this configuration dramatically.

For bleed configuration 4, the bleed mass flow is again on the order of $\dot{m}_{bleed}/\dot{m}_0 = 0.02 - 0.03$, lying between configurations 2 and 3. The mass flow is slightly higher than for configuration 2, based on the fact that the pressure level at the bleed location is slightly higher due to the reattachment pressure rise in this region. Because the pressure at the other end of the bleed gap is unchanged, a higher pressure difference leads to an increased bleed mass flow.

The total pressure recovery is difficult to measure because it is calculated from the static values at the upper and lower walls with the help of the already calculated Mach number at each pitot tube location. Thereafter, the single calculated pressure recoveries are mass-averaged; thus, the accuracy is very limited, but general conclusions can be drawn. The pressure recovery is plotted for the situation with no additional imposed backpressure; thus, it is not representing the maximum obtainable pressure recovery of the inlet. The total pressure recovery decreases slightly for the transition from configuration 0 to 1; this has been discussed in detail in [1]. For the other configurations 2–4, the total pressure recovery increases slightly.

B. Three-Dimensional Inlet, Width of 80 Millimeters, No Bleed

1. *Backpressure Ratio Variation with Different Throttle Degrees*

As for the 2-D case, the mass flow meter is also used to impose different backpressures on the internal flowfield of the 3-D scramjet compression system. The relation between the throttle degree Δ and the backpressure ratio can be seen in Fig. 7. Without any backpressure imposed by the mass flow meter $\Delta < 78\%$, the static pressure ratio at the position of the pitot rake is $p/p_\infty = 40$, which is an increase of +33% compared with the 2-D inlet. The pressure ratio generally increases with increasing throttling degree. However, the points scatter in the range of $79\% < \Delta < 84\%$, which is due to the strongly varying shock structures in the region of the pitot rake and the fact that all available static pressure values are plotted, which includes that with different pitot rake positions. Here, the reflected lip shock, the sidewall shocks, and the expansion fans lead to a very complex flow structure. For $\Delta > 85\%$, the flow at the defined combustion-chamber interface $x = 0.585$ m is completely subsonic. The backpressure ratio has to be considered more in a qualitative way than in a absolute way, because the pressure ratio in the interface plane is highly inhomogeneous. The blocking limit is for $\Delta > 86\%$ on the order of $p/p_\infty \approx 190 - 200$, which corresponds to the other investigated inlet configurations ([1] and Fig. 11).

2. *Static Wall and Pitot Rake Pressure Plots*

The internal flow is investigated by means of static pressure measurements along the centerline of the inlet. No shadowgraph pictures are available for the main part of the isolator, because of the metallic inserts. Shadowgraph pictures are only available at the vicinity of the lip where the separation bubble is visible. The main

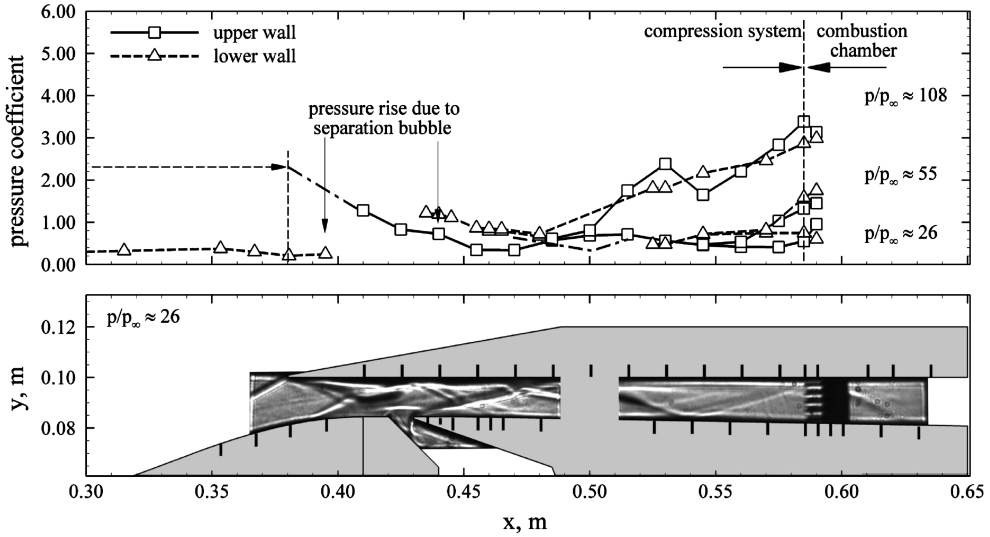

Fig. 6 Static wall pressures in the isolator for bleed configuration 4, including the theoretical pressure value at the lip tip computed by oblique shock theory, shadowgraph picture with no additional imposed backpressure $p/p_\infty = 30$.

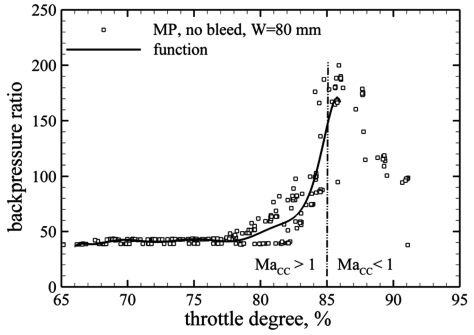

Fig. 7 Backpressure ratio as a function of throttling degree for the 3-D inlet with isolator width $W = 80$ mm (MP denotes measurement points).

flow structure in the x–y plane has been described here and extensively in [1] for the 2-D configuration without bleed. The general overlaying flow structure in the x–z plane is displayed in Fig. 8. The two sidewall compression shocks cross each other in the symmetry plane of the inlet. Further downstream, they interact with the expansions fans; that is, they are bent toward the walls and are reflected.

Comparing the static pressure profile in Fig. 8 with that for the 2-D inlet ($W = 100$ mm) as discussed in [1], two regions are of special interest.

A. Lip Area. Here ($0.350 \text{ m} < x < 0.470$ m), the first pressure measurement at the lip is very high ($c_{P,H1} = 3.5$) compared with the maximum value ($c_{P,H2} = 1.5$) for the $W = 100$ mm configuration. In addition, the pressure peak has moved upstream. This must be

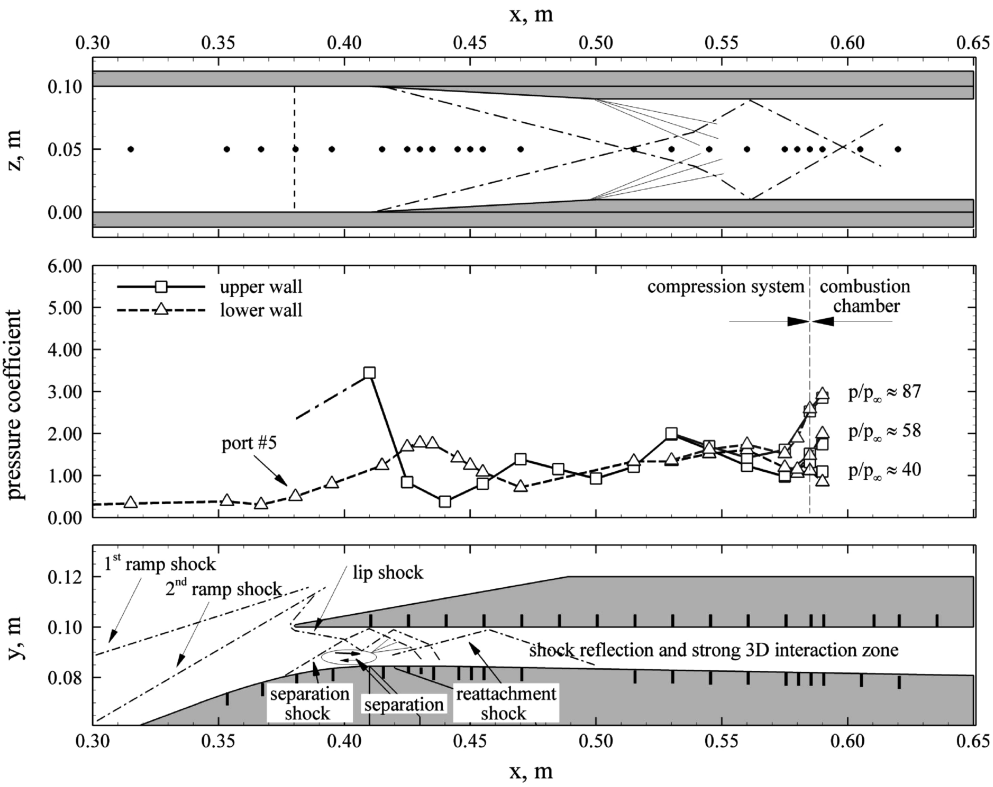

Fig. 8 Static wall pressure distribution on the upper and lower walls of the 3-D inlet with isolator width $W = 80$ mm and different imposed backpressure ratios.

based on the fact that the lip-shock-induced separation bubble has moved upstream and the separation-induced shock interacts further upstream with the upper-wall boundary layer. That the separation bubble has moved upstream is confirmed by looking at the ramp pressure distribution. The first four displayed pressure ports ($R2$–$R5$) decrease for the $W = 100$ mm configuration based on the curvature of the ramp. The pressure value at the pressure port $R5$, in contrast, rises for the $W = 80$ mm configuration and indicates that the separation bubble has already propagated upstream up to this point. Furthermore, the highest pressure values corresponding to the reattachment-shock location on the lower wall are near $x = 0.430$ m and not near $x = 0.450$ m, as in the basic configuration [1].

B. Isolator Exit Area. In this part ($0.510 \text{ m} < x < 0.600$ m), the secondary shock and expansion fan structure are notable. Especially, the upper-wall static pressure starts to rise near $x = 0.520$ m and is not further decreasing, as in the compared configuration. This is based on the fact that the sidewall compression shocks interact with the centerline near this point. The static wall pressure increases on the upper and lower walls up to $x = 0.530$ m. Further downstream, the effects of the expansion fans are clearly visible. The pressure decreases up to slightly upstream of the pitot rake and remains almost constant in the rest of the investigated area at a backpressure level of $p/p_\infty \approx 40$.

Increasing the backpressure leads to a static pressure rise further upstream, resulting from the developing shock train. But the upstream propagation is far more limited than in the other discussed cases (see the preceding discussion and [1]). This is clearly related to the fact that the inlet delivers a higher pressure ratio to the combustion-chamber interface, and an increase in imposed backpressure ration can be accomplished with a much shorter shock train.

Even though the flow structure is very complex, the pitot pressure profiles at the end of the isolator are very symmetric. This is surprising, especially because the symmetry remains even for different backpressure ratios (see Fig. 9a). The calculated Mach numbers are just to give an idea of the order of magnitude (see Fig. 9b). The Mach number without any additional imposed backpressure has decreased to $M = 2.1$, compared with the 2-D case with $M = 2.7$. This is obvious because the obtained backpressure ratio for the 3-D inlet configuration is higher, resulting in a lower Mach number. Obviously, the flow is not symmetric in the combustion-chamber interface y–z plane. This was checked by positioning the pitot rake 25 mm out of the symmetry plane in both directions. The resulting pitot pressure profiles and Mach number profiles in all three planes [$z = 25, 50\,(C/L)$, and 75 mm] are plotted in Figs. 10a and 10b. The measured profiles at offcenter planes are almost identical, which indicates a symmetric flow to the center plane of the isolator, but the difference to the centerline profile is obvious. Because the flow structure is very complex, especially in the strong 3-D interaction regime in the internal contraction part of the inlet, more detailed investigation have to be supported by 3-D CFD calculations. This includes crossing shocks in different planes; shock reflection on the upper/lower and sidewalls; boundary-layer development and separation; corner flows, including development of corner vortices; etc.

For this configuration, the mass budget for the configuration without bleed and with are summarized in Table 5. The spill is assumed to be constant, although the separation bubble on the ramps has propagated slightly upstream, as discussed earlier. The mass capture ratio is approximately the same as for the 2-D configuration, because the external flow structure has not changed. The same is true for the bleed mass flow, which should be in the same order because the internal sidewall compression ramps start at the same x position as the bleed gap: $x = 0.410$ m. This means that the bleed flow is still mainly affected by the lip shock and not the sidewall shocks, consequently leading to the same mass flow.

C. Three-Dimensional Inlet, Width of 70 Millimeters, No Bleed

1. Backpressure Ratio Variation with Different Throttle Degrees

The relation between the throttle degree Δ and the backpressure ratio for the $W = 70$ mm configuration can be seen in Fig. 11. Without any backpressure imposed by the mass flow meter $\Delta < 79\%$, the static pressure ratio at the position of the pitot rake is

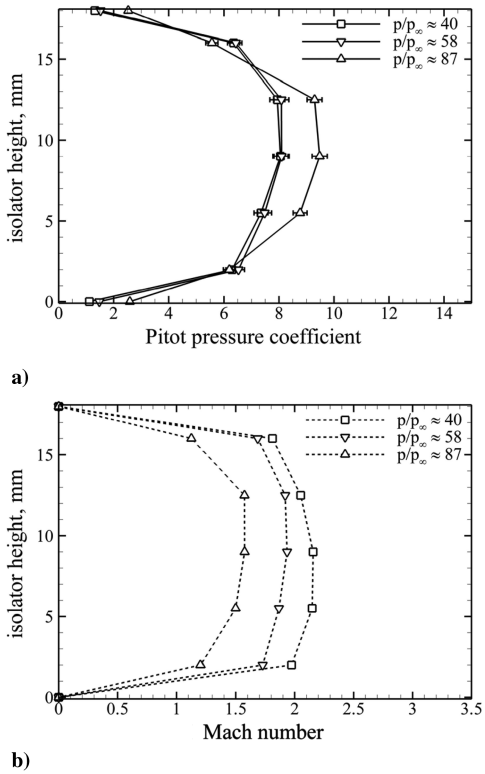

Fig. 9 Pitot-pressure profiles and calculated Mach number profiles for the width $W = 80$ mm configuration without bleed and different backpressure ratios.

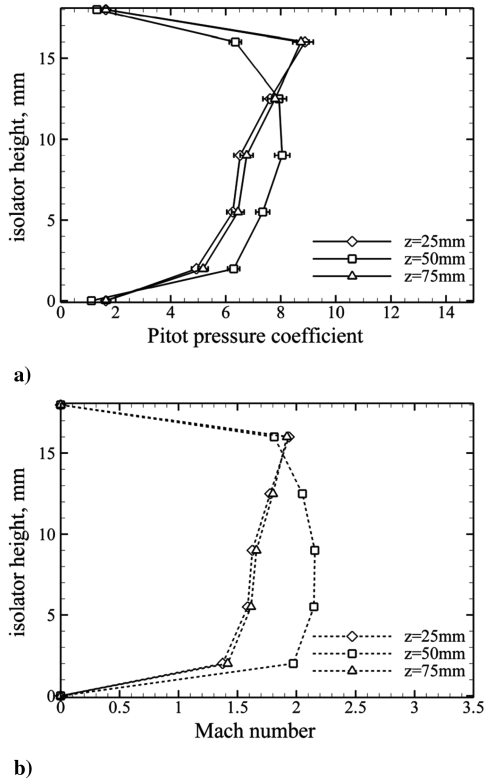

Fig. 10 Pitot-pressure profiles and calculated Mach number profiles for the width $W = 80$ mm configuration without bleed at three different positions along the isolator width.

Table 5 Breakdown of the different inlet mass flows and total pressure recovery

	Mass flow rate			π
α, deg	MCR	Bleed mass flow ratio	Spill mass flow ratio	p_{t3}/p_{t0}
0	$0,72 \pm 2,8\%$	0	0.28	0.085
0	$0,71 \pm 2,8\%$	Configuration 1 ~0.01	0.28	0.094

$p/p_\infty = 53$, which is an increase of +75% compared with the 2-D inlet. The pressure ratio generally increases with increasing throttling degree. However, the backpressure rises only moderately in the throttle range of $0\% < \Delta < 84\%$, based on the already high pressure delivered by the inlet. The backpressure ratio increases very fast in the throttle degree range $84\% < \Delta < 86\%$, and the flow turns subsonic for $\Delta > 86\%$ at the defined combustion-chamber interface $x = 0.585$ m. This means that the isolator can only compensate a smaller backpressure increase than in the other investigated cases. But, of course, because the inlet delivers a higher pressure ratio to the isolator interface (and assuming a constant needed combustion-chamber pressure in all cases), the isolator only has to compensate a very small (if any) pressure increase. The blocking limit is for $\Delta > 87\%$ on the order of $p/p_\infty \approx 200$, which corresponds to the other investigated inlet configurations (see [1] and Fig. 7).

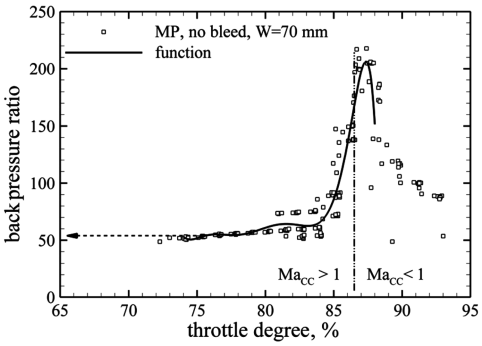

Fig. 11 Backpressure ratio as a function of throttling degree for the 3-D inlet with isolator width $W = 70$ mm.

2. Static Wall and Pitot-Rake Pressure Plots

The flow structure looks very similar to the preceding investigated configuration. The effects, in principle, are the same. The sidewall shocks are stronger and cross each other further upstream, based on the increased sidewall compression angle. Again comparing the static pressure profile (Fig. 12) with that for the 3-D inlet ($W = 80$ mm) already discussed (Fig. 8 and the 2-D inlet [1]), two regions are of special interest.

A. Lip Area. The higher internal compression ($0.350 \text{ m} < x < 0.470$ m) leads to a further upstream propagation of the separation bubble. This is evident by looking at pressure port 5 on the ramp (see Fig. 12). This pressure value has notably increased compared with Fig. 8. The decrease in pressure peak at the first pressure port close to the lip ($c_{P,H1} = 2.8$) can only be explained by the variation in shock-impinging location. The rest of the flow structure is quite the same for both 3-D inlets.

B. Isolator Exit Area. In this part, the secondary shock and expansion fan structure is notable. Especially, the upper-wall static pressure starts to rise near $x = 0.490$ m and is not decreasing subsequently, as is the case in the 2-D configuration. The rise occurs further upstream, is steeper, and leads to a considerably higher static pressure level (see Fig. 12) than in the previous case, because the sidewall compression shocks are steeper. This is based on the fact that the Mach number is more or less unchanged up to $x = 0.410$, but

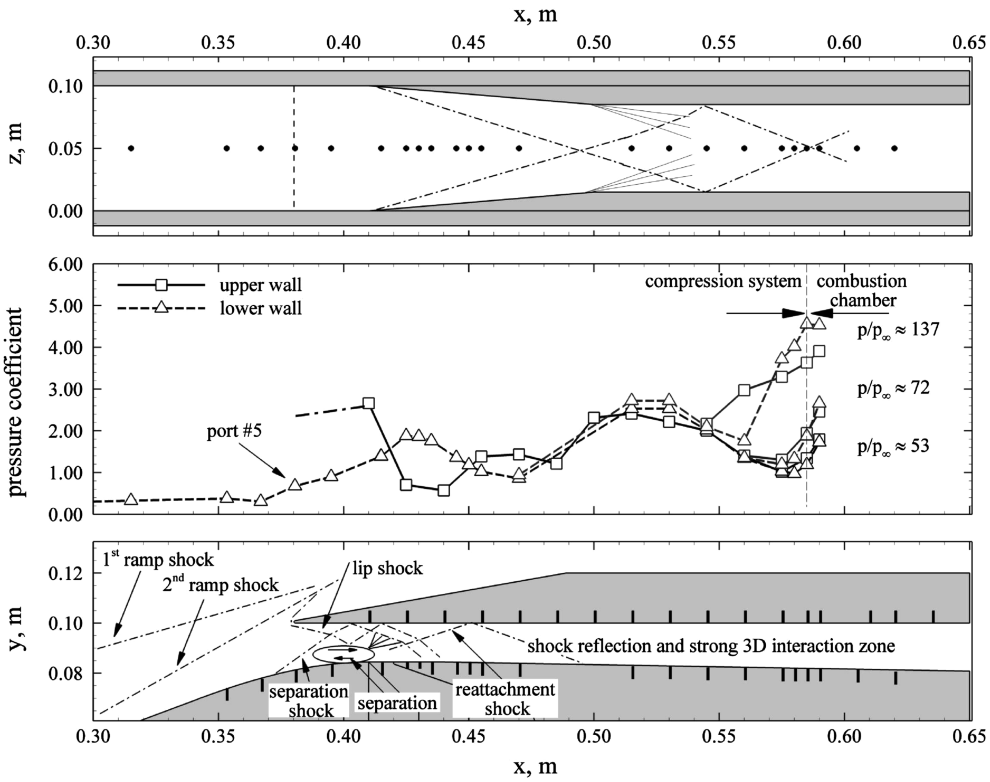

Fig. 12 Static wall pressure distribution on the upper and lower walls of the 3-D inlet with isolator width $W = 70$ mm and different imposed backpressure ratios.

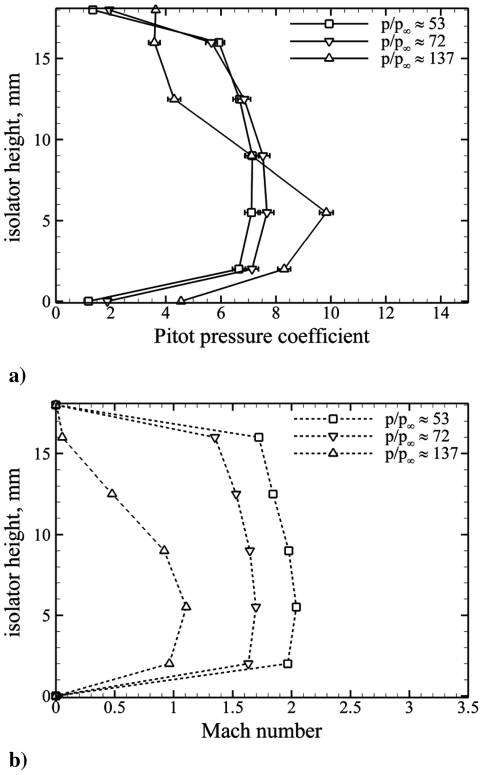

Fig. 13 Pitot-pressure profiles and calculated Mach number profiles for the width $W = 70$ mm configuration without bleed and different backpressure ratios.

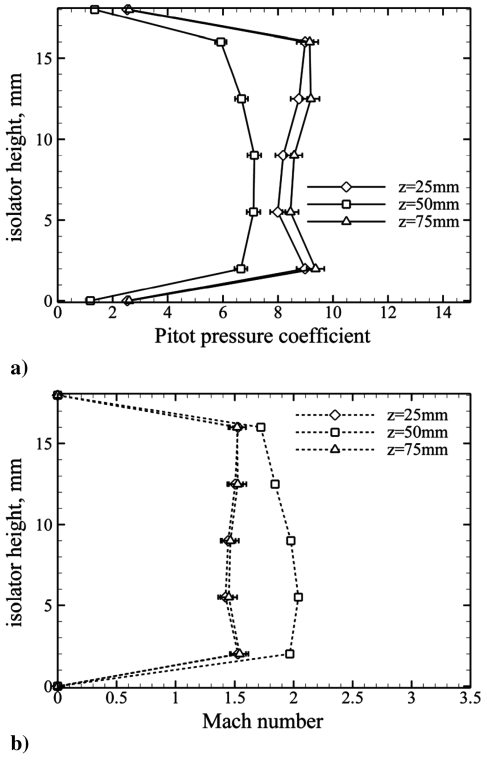

Fig. 14 Pitot-pressure profiles and calculated Mach number profiles for the width $W = 70$ mm configuration without bleed at three different positions along the isolator width.

the sidewall compression-ramp angle is higher, leading to a stronger shock; thus, the interaction at the centerline is more upstream. The static wall pressure increases on the upper and lower walls up to $x = 0.530$ m. Further downstream, the effects of the expansion fans are clearly visible. The pressure decreases until shortly in front of the pitot rake ($x = 0.570$ m). Thereafter, the pressure rises again which indicates that the reflected sidewall shocks cross each other again in this area, leading to a backpressure ratio level of $p/p_\infty \approx 53$.

The pitot pressure profiles at the end of the isolator are very symmetric. The pitot pressure remains almost unchanged for the first two backpressure ratios. For the next backpressure level, the pitot profile becomes asymmetrical and a large subsonic zone develops in the upper half of the isolator (see Fig. 13a). As already noted, the calculated Mach numbers are just to give an idea of the order of magnitude (see Fig. 13b). The Mach number without any additional imposed backpressure further decreased to $M = 2.0$, because the obtained pressure ratio is further increased, compared with the 2-D case with $M = 2.7$ and the $W = 80$ mm configuration (see Fig. 9).

Obviously, the flow is not symmetric in the combustion-chamber interface y–z plane. This was again checked by positioning the pitot rake 25 mm out of the symmetry plane in both directions. The resulting pitot pressure profiles and Mach number profiles in all three planes ($z = 25$, 50 (C/L), and 75 mm) are plotted in Figs. 14a and 14b. The measured profiles in the out-of-center plane and the center plane differ. But as in the previous configuration, the profiles are almost identical for the out-of-center plane, which indicates a symmetric flow to the center plane of the isolator.

The mass budget for this configuration without bleed and with bleed are summarized in Table 6. The spill is assumed to be constant, although the separation bubble on the ramps has propagated considerably upstream, as discussed earlier. But the shadowgraphs indicate that the external shock structure is unchanged. As noted, the mass capture ratio is approximately the same as for the 2-D configuration, based on the same rational. The total pressure recovery is further decreased based on the stronger shocks introduced by the sidewall compression ramps compared with the configuration with $W = 80$ mm.

D. Direct Comparison of the Static Wall Pressure for Different Internal Contraction Ratios

To summarize the differences in the internal flowfield of the preceding discussed three different internal contraction ratios, the static pressure distributions $0.350\ \text{m} < x < 0.600$ m for these configurations are combined in one graph in Fig. 15 for the isolator upper wall and lower wall. The increase in separation-bubble size (1) on the ramp and the stronger interaction with the upper wall (2) is visible in the region $0.370 < x < 0.420$ m as well as the stronger interaction at the reattachment location (3) at the lower wall near $0.420 < x < 0.445$ m. Also, the reattachment shock impinges on the upper wall further upstream (4). The crossing shocks induced by the sidewall compression inlays lead to a pressure rise at the centerline, compared with the 2-D configuration. The upstream propagation of this interaction (5) is shown in the region $0.490 < x < 0.560$ m, as well as the pressure rise at the defined interface to the combustion chamber at $x = 0.585$ m.

Table 6 Breakdown of the different inlet mass flows and total pressure recovery

	Mass flow rate			π
α, deg	MCR	Bleed mass flow ratio	Spill mass flow ratio	p_{t3}/p_{t0}
0	$0,72 \pm 2,8\%$	0	0.28	0.073
0	$0,70 \pm 2,8\%$	Configuration 1 ∼0.02	0.28	0.068

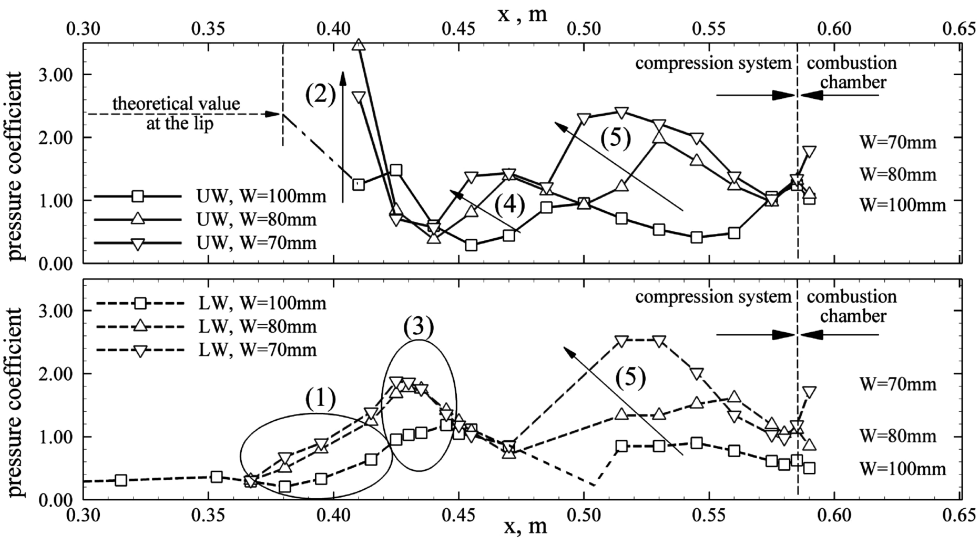

Fig. 15 Static pressure distribution for different internal contraction ratios (UW is the upper wall and LW is the lower wall).

V. Conclusions

The main goal of this experimental study was to investigate the influence of different bleed configurations and internal contraction ratios on the performance of previously investigated inlets. Therefore, the 2-D configuration was first investigated for various bleed configurations. The main objective of the bleed (i.e., to eliminate the separation bubble) can be achieved with a 10-mm bleed gap. Further increase of size of the bleed gap up to 20 mm does not lead to a general change in flow structure and no significant improvement in pressure recovery. But the removed mass flow is increased disproportionately to the gap size increase. Further, the significance of the correct bleed location for the effectiveness of the bleed and the overall design was demonstrated. Placing the bleed gap near the location of the inviscid shock-impinging location does not lead to the desired reduction in separation-bubble size, because the shock impinges on the ramp (due to the interaction with the thick-ramp boundary layer) considerably upstream of the bleed gap. This leads to a separation despite the existence of the bleed.

To address the question how far the internal contraction limit can be raised, sidewall compression ramps were introduced into the internal part of the inlet. It could be demonstrated that the internal contraction ratio can be extended over the Kantrowitz limit as detailed in [13]. But these configurations cause a further increase of the separation bubble in the throat area and its propagation upstream. The effects were significant in terms of a change in internal static pressure distribution but did not lead to inlet unstart under the investigated conditions. The introduced internal sidewall compression could be an option if several single engines have to be placed next to each other (e.g., for mechanical, fuel injection, thermal reasons, etc.). The present investigation shows that the inlet is still self-starting and the reduced isolator length is able to compensate different backpressure ratios. Of course, the flow structure is much more complex than for the 2-D case, but should be manageable if the sidewall compression is moderate, as in the presented cases. During this study no unexpected effects such as subsonic flow at the end of the isolator, backpressure behavior, sudden blocking of the inlet, unstartable inlet, etc., were discovered. Detailed investigation of such complex flowfield has to be supported by 3-D CFD calculations, which should use the presented data for the validation and selection of proper turbulence models. Finally, the CFD results in combination with the experimental data can be used to display and discuss the full 3-D flow details present in hypersonic inlets.

Acknowledgments

The financial support by the German National Research Council (DFG) within the research training group 1095/1 and the DLR, German Aerospace Center in Cologne is acknowledged. We would further like to thank P. Herzog and D. Lütz for their assistance during the experiments and P. Gruhn for his support during the analysis of the test results and the preparation of the paper.

References

[1] Häberle, J., and Gülhan, A., "Investigation Two-Dimensional Scramjet Inlet Flowfield at Mach 7," *Journal of Propulsion and Power*, Vol. 24, No. 3, May–June 2008, pp. 446–459. doi:10.2514/1.33545

[2] Häberle, J., and Gülhan, A., "Investigation of the Performance of a Scramjet Inlet at Mach 6 with Boundary Layer Bleed," AIAA Paper 2006-8139, 2006.

[3] Anderson, B. H., "Design of Supersonic Inlets by a Computer Program Incorporating the Method of Characteristics," NASA TN-D-4960, 1968.

[4] Schulte, D., Henckels, A., and Neubacher, R., "Manipulation of Shock/Boundary-Layer Interactions in Hypersonic Inlets," *Journal of Propulsion and Power*, Vol. 17, No. 3, May–June 2001, pp. 585–590.

[5] Shih, T.I-P., Rimlinger, M. J., and Chyu, W. J., "Three-Dimensional Shock-Wave/Boundary-Layer Interaction with Bleed," *AIAA Journal*, Vol. 31, No. 10, Oct. 1993, pp. 1819–1826.

[6] Harloff, G. J., and Smith, G. E., "Supersonic Inlet Boundary-Layer Bleed Flow," *AIAA Journal*, Vol. 34, No. 4, Apr. 1996, pp. 778–785.

[7] Billig, F. S., and Kothari, A. P., "Streamline Tracing: Technique for Designing Hypersonic Vehicles," *Journal of Propulsion and Power*, Vol. 16, No. 3, 2000, pp. 465–471.

[8] Billig, F. S., "Research on Supersonic Combustion," *Journal of Propulsion and Power*, Vol. 9, No. 4, 1993, p. 499.

[9] Heiser, W. H., and Pratt, D. T., *Hypersonic Airbreathing Propulsion*, AIAA Education Series, AIAA, Reston, VA, 1993.

[10] Sugiyama, H., Minato, R., Mizobata, K., Tojo, A., and Muto, Y., "Study on Shock Wave and Turbulent Boundary Layer Interactions in a Square Duct at Mach 2 and 4," *Journal of Thermal Science*, Vol. 15, No. 1, 2006, pp. 37–42. doi:10.1007/s11630-006-0037-3

[11] Herrmann, C. D., and Koschel, W. W., "Experimental Investigation of the Internal Compression of a Hypersonic Intake," AIAA Paper 2002-4130, 2002.

[12] Reinartz, B. U., Herrmann, C. D., Ballmann, J., and Koschel, W. W., "Aerodynamic Performance Analysis of a Hypersonic Inlet Isolator Using Computation and Experiment," *Journal of Propulsion and Power*, Vol. 19, No. 5, 2003, pp. 868–875.

[13] Kantrowitz, A., and Donaldson, C. D., "Preliminary Investigation of Supersonic Diffusers," NACA ACR L5D20, 1945.

[14] Holland, S. D., and Murphy, K. J., "An Experimental Parametric Study of Geometric, Reynolds Number and Ratio of Specific Heats Effects in Three-Dimensional Sidewall Compression Scramjet Inlets at Mach 6," AIAA Paper 93-0740, 1993.

[15] Holland, S. D., "Mach 10 Experimental Database of a Three-Dimensional Scramjet Inlet flowfield," NASA TM 4648, Sept. 1995.

[16] Tani, K., Kanda, K., Kudou, K., Murakami, A., Komuro, T., and Itoh, K., "Aerodynamic Performance of Scramjet Inlet Models with a Single

Strut," 31st Aerospace Sciences Meeting and Exhibit, Reno, NV, AIAA Paper 93-0741, 1993.
[17] Zuber, M. E., Dieudonné, W., and Charbonnier, J-M., "Flowfield Structure for Crossing Shocks Intersecting a Mach 6 Laminar Boundary Layer," 18th AIAA Applied Aerodynamics, Denver, CO, AIAA Paper 2000-4515, 2000.
[18] Goonko, Y. P., Latypov, A. F., Mazhul, I. I., Kharitonov, A. M., and Yaroslavtsev, M. I., "Structure of Flow over a Hypersonic Inlet with Side Compression Wedges," *AIAA Journal*, Vol. 41, No. 3, Mar. 2003, pp. 436–447.
[19] Jin, Z. G., and Zhang, K. Y., "Experimental Investigation of a Three-Dimensional SCRAM Jet Inlet Tested in High Enthalpy Impulse Wind Tunnel at Mach 6," Inst. of Space and Astronautical Science Paper 2005-1110, 2005.
[20] Walker, S. H., "Hypersonic Collaborative Australia/United States Experiment (HYCAUSE)," AIAA Paper 2005-3254, 2005.
[21] Ho, S. Y., "Thermal-Structural Analysis of the DARPA HYCAUSE 3-D Engine for Flight Test," AIAA Paper 2006-8070, 2006.
[22] Smart, M. K., "Experimental Testing of a Hypersonic Inlet with Rectangular to Elliptical Shape Transition," *Journal of Propulsion and Power*, Vol. 17, No. 2, Mar.–Apr. 2001, pp. 276–283.
[23] Smart, M. K., and Trexler, C. A., "Mach 4 Performance of Hypersonic Inlet with Rectangular to Elliptical Shape Transition," *Journal of Propulsion and Power*, Vol. 20, No. 2, Mar.–Apr. 2004, pp. 288–293. doi:10.2514/1.1296
[24] Smart, M. K., and White, J. A., "Computational Investigation of the Performance and Backpressure Limits of a Hypersonic Inlet," 40th AIAA Aerospace Sciences Meeting and Exhibit, Reno, NV, AIAA Paper 2002-0508, 2002.
[25] Merzkirch, W., *Flow Visualisation*, Academic Press, New York, 1974.
[26] Triesch, K., "Verwendung von Kegeldüsen zur Drosselung und Durchsatzmessung bei Überschalleinläufen," DLR, German Aerospace Center Rept. IB-39113-83-A-04, Cologne, Germany, 1983.
[27] "Durchflussmessung mit Blenden, Düsen und Venturirohren in voll Durchströmten Rohren mit Kreisquerschnitt," German Inst. for Standardization, Standard DIN 1952, Beuth–Verlag, Berlin, 1982
[28] Lin, K. C., Tam, C. J., Jackson, K. R., Eklund, D. R., and Jackson, T. A., "Characterization of Shock Train Structures inside Constant Area Isolators of Model Scramjet Combustors," 44th AIAA Aerospace Sciences Meeting, Reno, NV, AIAA Paper 2006-816, 2006.
[29] Schulte, D., Henckels, A., and Neubacher, A., "Manipulation of Shock/Boundary-Layer Interactions in Hypersonic Inlets," *Journal of Propulsion and Power*, Vol. 17, No. 3, May–June 2001., pp. 585–590.
[30] Hermann, D., Triesch, K., and Gülhan, A., "An Experimental Study of Chin-Intakes for Airbreathing Missiles with High Agility," *Journal of Propulsion and Power* (to be published); also AIAA Paper 2007-5423, 2007.
[31] Krause, M., and Ballmann, J., "Numerical Simulations and Design of a Scramjet Intake Using Two Different RANS Solvers," AIAA Paper 2007-54232007.

R. Bowersox
Associate Editor